p-ISSN 2089 – 0133 e-ISSN 2477-6416
URL : https://jurnal.uns.ac.id/ijap/article/view/76131
Indonesian Journal of Applied Physics (IJAP) Vol. 13 No. 2 page 289
DOI : https://doi.org/10.13057/ijap.v13i2.76131

ESTIMATING SURFACE CURRENT FROM HIMAWARI-8 SST DATA USING PARTICLE IMAGE VELOCIMETRY METHOD (CASE STUDY IN THE FLORES SEA)

Kadek Setiya Wati *[1], Takahiro Osawa[2], I Wayan Gede Astawa Karang[3]
[1]1Meteorological Climatological and Geophysical Agency (BMKG), Denpasar, Indonesia
[2] Center of Research and Application of Satellite Remote Sensing (YUCRAS), Yamaguchi University, Ube-shi Yamaguchi Japan
[3]Departement of Marine Sciences, Faculty of Marine Science and Fisheries, Udayana University, Denpasar, Indonesia
*kadek.setiya@gmail.com

Received 07-06-2023, Revised 10-08-2023, Accepted 08-10-2023
Available Online 08-10-2023, Published Regularly October 2023

ABSTRACT

Four High-Frequency radar systems (HF) have been installed in Indonesia to monitor surface currents. In-situ ocean current observations are relatively expensive and limited by spatial and temporal resolution. Satellite remote sensing enables the estimate of surface current data generally from surface tracer data, including sea surface temperature (SST). Various methodologies have been developed to obtain surface currents. With Himawari-8 SST data, this study examines the accuracy of the resulting estimation. The cross-correlation fields of two identical-sized interrogation windows obtained from sequential images are employed in Particle Image Velocimetry (PIV). The HF radar in Labuan Bajo was used to validate surface current velocity estimates. RMSE, bias, and the Willmott index determined the accuracy. According to the estimates of surface currents made on July 29, 2022, the results follow a monsoon-characteristic wind pattern in the Flores Sea. HF radar observations better validate the V component current estimation than the U component current estimation. A study of sea surface currents from SST data is lacking in Indonesian seas, and more repetition is required. As a result, This method has the potential can be employed to observe aquatic environments in other Indonesian areas.

Keywords: PIV; HF radar; current velocity; ocean current; remote sensing

Cite this as: Wati, K. S., Osawa, T., & Karang, I. W. G. A. 2023. Estimating Surface Current from Himawari-8 SST Data Using Particle Image Velocimetry Method (Case Study in The Flores Sea). *IJAP: Indonesian Journal of Applied Physcis, 13*(2), 289-304. doi: https://doi.org/10.13057/ijap.v13i2.76131

INTRODUCTION

Understanding surface currents is necessary because most human activity in the oceans occurs at the surface, and surface currents influence it. Surface currents are a central topic in operational oceanography, with rapidly expanding observation and forecasting capabilities. Observations now provide sufficient detail, and numerical models can predict applications that use surface current information to aid marine safety, value creation, and environmental monitoring. The Global Ocean Observing System (GOOS) and Ocean Observations Panel for Climate (OOPC) identify surface currents as one of the Essential Ocean Variables (EOV)[1].

Observations of real-time ocean surface currents allow search and rescue at ocean disaster sites and research into ocean contaminants surface transport. Although real-time surface currents have been mapped by High-Frequency (HF) radar, shipboard instruments, satellite altimetry, and surface drifters[2], surface current processes are more difficult to resolve using in situ data due to two types of issues. First and most importantly, the limitations of temporal and spatial resolutions prevent us from calculating precise surface currents. Second, collecting in-situ data is expensive and time-consuming[3].

The development of satellite remote sensing enabled a significant breakthrough in generating surface currents[2]. Depending on the type of satellite data, there are two main approaches to satellite remote sensing in estimating current velocity[4]. The first derives the geostrophic current from the sea surface height. The second employs two consecutive (in time) images in the infrared (e.g., SST) or visible (e.g., chlorophyll-a concentration) bands[5].

Various methodologies and approaches have been presented over the last few decades to derive surface currents from surface tracers such as sea surface temperature (SST) or ocean colour (OC)[6]. Some techniques assume dynamical restraint on the SST images[7-10]. Others are based on pattern recognition techniques such as neural networks[11-13] as Maximum Cross Correlation [5, 14-15] or as Particle Image Velocimetry[2, 16-17].

This research employed the Particle Image Velocimetry (PIV) method to create a velocity field close to the ocean's surface using Himawari-8 SST data. PIV is a standard experimental strategy that generates an instantaneous velocity field in the laboratory by illuminating particles (here, equivalent to scalar tracers' SST or Chl-a) in a cross-section of a water channel (here, satellite coverage) with a laser sheet (here, the sun) and recording particle movement with a camera (herein, a satellite sensor). The PIV algorithm generates a cross-correlation plane by taking the FFT between two identically sized interrogation windows obtained individually from two successive images. An optimized displacement vector is determined to maximize image matching[2]. In the oceanographic environment, large-scale PIV can be used to determine sea surface flow conditions. To provide enough data for consistent in situ validation, high-resolution temporal LSPIV observations are required. Accurate measurements of sea surface flow directions can be obtained with negligible wind effects. ADCP's consistent in-field observations revealed that both systems agree[17].

Due to the limited real-time observation of surface currents in Indonesia, Himawari-8 SST data and the PIV method were applied in this study. Currently, surface current observations in real-time are made using HF radar installed at 4 locations, including the Flores Sea. Research on ocean surface currents from SST data has not been widely conducted in the Indonesian region. This is because SST in the Indonesian area generally tends to be uniform. Therefore, this study was conducted to determine the accuracy of SST satellite data in generating ocean current surface velocity in the Indonesian region. This strategy can be applied to other areas in Indonesia that do not yet have an in-situ marine observation network.

METHOD

The Flores Sea will serve as the location for the investigation; its coordinates range from 7.5 S to 9.0 S and 119 E to 123 E. It borders the Bali Sea on the West and the Banda Sea on the East. These two seas form the boundary of the Flores Sea. Meanwhile, Sulawesi is located in the north of this region, while Flores is located in the south. The region surrounding this area is home to one of Indonesia's most renowned tourist destinations, Komodo National Park. The research area is illustrated in Figure 1. At this location, studies of ocean surface currents have

not been widely conducted[18-19]. The research period is July 29, 2022, at 00.00 - 23.20 UTC. It was decided to conduct the research when there would be little cloud cover—satellite imagery to be obtained of the study area clearly and precisely.

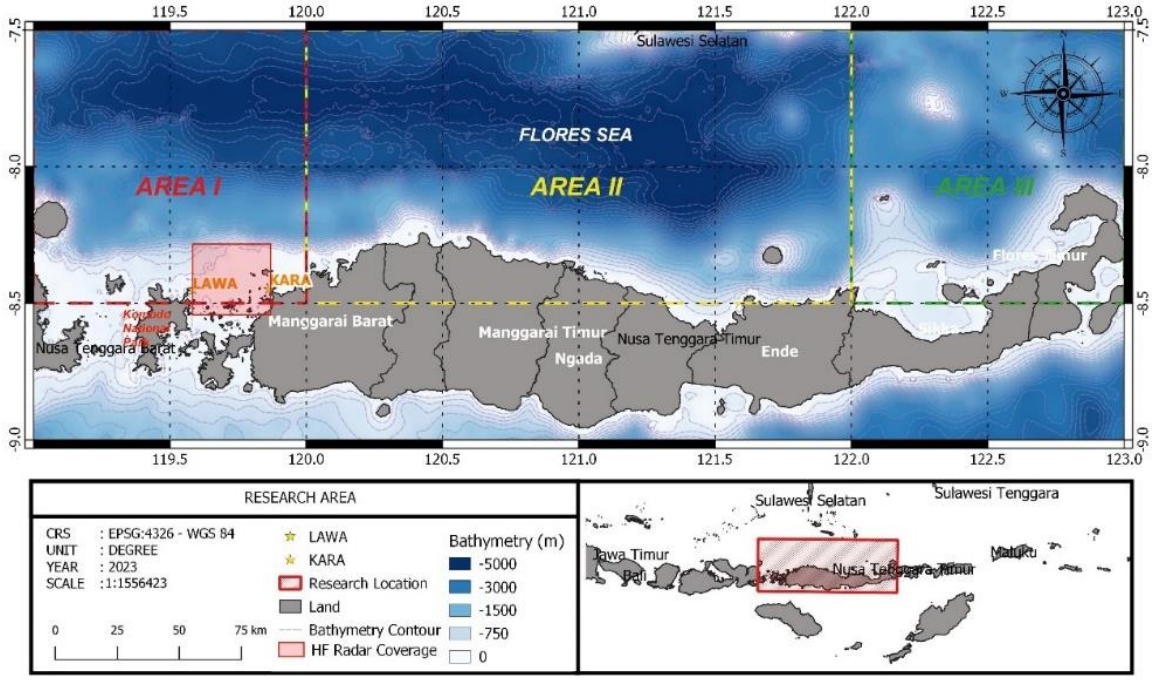

Figure 1. Research Area. The pink box is the validation area. The segmented area around the Flores Sea is Area I (red dash line) in the western part, Area II (yellow dash line) in the central part, and Area III (green dash line) in the eastern part.

The Japan Aerospace Exploration Agency (JAXA) offers Himawari-8 AHI skin SST products (at approximately 10 µm depth) estimated from 10.4, 11.2, and 8.6 µm radiances in near real-time[20]. The SST data used is level 2 data with a time resolution of 10 minutes and a spatial resolution of 2 km. The data were produced by JAXA Himawari Monitor System and downloaded from the website http://www.eorc.jaxa.jp/ptree/index.html.

Because of its use of average velocity in interrogation areas utilizing correlation functions, particle image velocimetry (PIV) is widely used in various research fields. An interrogation window in PIV subsamples two sequential digital pictures, and the correlation peak location is proportional to particle displacement. The average velocity of particles within these interrogation windows can be calculated using the following formula[21]:

$$\vec{v} = \frac{\Delta \vec{X}}{\Delta t} \quad (1)$$

Where:

$\Delta \vec{X}$ is the average spatial shift;

Δt is the time interval between two sequential images.

The interrogation area (IA) in the first image and the interrogation areas in a search area (SA) in the second image are calculated using cross-correlation. The pair of particles with the highest

cross-correlation coefficient is chosen as a candidate vector[22]. Equation 2 shows cross-correlation[23]:

$$\boldsymbol{R(s,t) = \frac{1}{N^2}\sum_{j=0}^{N-1}\ \sum_{j=0}^{N-1}\ F'_{I,J}(i,j)F''_{I,J}(i+s,j+t)} \quad (2)$$

Where R denotes the recurrent cross-correlation between sub-windows I, J in the first image of the image pair (F') and the next image of the image pair (F''), i j the pixel location within sub-window I, J, and s, t denotes the 2-D cyclic lag for that cross-correlation computing.

For discrete data, the Fourier transform is efficiently implemented using the Fast Fourier transform, which reduces computation operations. Furthermore, subpixel peak detection methods using Gaussian fitting are applied to the cross-correlation distribution to improve measurement accuracy[22]. This study uses a multipass scheme interrogation window: pass 1: 128 x 128, pass 2: 64 x 64, and pass 3: 32 x 32 with 50% overlap. All analysis processes are conducted using the PIVlab software.

Post-processing techniques can increase PIV performance. The existence of incorrect vectors lowers the quality of the results since it makes interpretation more complicated and, in some situations, precludes derived flow magnitudes from being obtained. As a result, data validation techniques capable of detecting false vectors automatically are necessary before the post-processing chain can begin[24]. This work employs median filtering to detect and remove spurious vectors. The filter compares velocity fluctuations to the neighbourhood median in 3.3 regions surrounding the primary vector. The median of this variance is then used to normalize a more typical median test. Smoothing data can also be used effectively to reduce noise. The smoothing methods use a penalized least squares method to reduce the difference between analytical and actual velocities. As a result, it was decided to add this approach to PIVlab to improve velocity prediction accuracy(25).

Data observations of ocean surface currents from HF radar are used. Figure 2 shows the two-point location and coverage area of the Labuhan Bajo HF radar. HF radar data in the Flores Sea were obtained from the BMKG Maritime Meteorological Center.

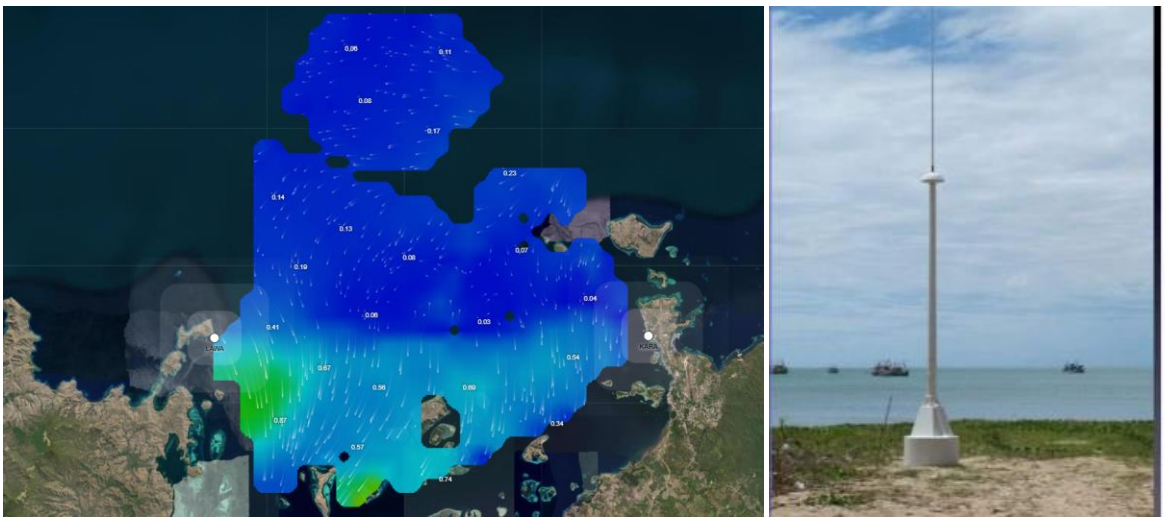

Figure 2. HF radar location in Labuhan Bajo. HF radar LAWA on the left and HF radar KARA on the right. The blue color represents surface current data captured by HF radar LAWA and KARA (left figure). Example of HF radar antenna(18) (right figure).

Table 1. Labuhan Bajo HF Radar Specifications

	LAWA	**KARA**
Operating Frequency	13 MHz	13 MHz
Spatial Resolution	1 km	1 km
Temporal Resolution	20 minutes	20 minutes

The calculations conducted to get the value of ocean current speed using Equation 3[18]:

$$\boldsymbol{curr} = \sqrt{\boldsymbol{u^2 + v^2}} \quad (3)$$

Where:
The curr is current sea speed (m/s)
u is the zonal current (m/s)
v is the meridional current (m/s)

To get the value of current sea direction (θ) is also calculated using the following Equation 4[18]:

$$\boldsymbol{\theta} = \boldsymbol{arctan}\frac{\boldsymbol{v}}{\boldsymbol{u}} \quad (4)$$

Where:
θ is the current sea direction (degree)
u is the zonal current (m/s)
v is the meridional current (m/s)

An accuracy assessment is done on the current velocity of the U and V components. The PIV method estimation results are compared with HF radar observations. Estimation results are selected every 20 minutes to match the HF radar temporal resolution. The difference in spatial resolution between Himawari-8 SST data and HF radar results in differences in coordinate points in the resulting U and V components. Therefore, the next step is to adjust the HF radar coordinates. In this process, natural neighbor interpolation (NNI) is used.

The magnitude of measurement error determines the accuracy of an estimated surface velocity. The PIV method has two types of error sources: bias error and RMSE[26]. The bias error (ϵbias) determines the trueness of the estimated displacement[27], while the RMSE calculates the precision of the estimated displacement.

The statistical equation used for RMSE and bias error calculation is expressed below[26]:

$$\boldsymbol{\epsilon_{rms}} = \sqrt{\frac{\boldsymbol{1}}{\boldsymbol{n}}\sum_{\boldsymbol{i=1}}^{\boldsymbol{n}} \left(\boldsymbol{d}_{\text{mean}} - \boldsymbol{d}_{\text{estimated},\boldsymbol{i}}\right)^{\boldsymbol{2}}} \quad (5)$$

$$\boldsymbol{\epsilon}_{\text{bias}} = \frac{\boldsymbol{1}}{\boldsymbol{n}}\sum_{\boldsymbol{i=1}}^{\boldsymbol{n}} \boldsymbol{d}_{\text{estimated},\boldsymbol{i}} - \boldsymbol{d}_{\text{true value}} \quad (6)$$

Where $d_{estimated,i}$ is the displacement estimated by PIV at observation i, d_{true} value is the actual displacement, d_{mean} is the mean of estimated displacement, and n is the total number of observations. In addition, the Willmott index of agreement is also used with the following formula[28]:

$$d = 1 - \frac{\sum_{i=1}^{n} (P_i - O_i)^2}{\sum_{i=1}^{n} (|P_i - \bar{O}| + |O_i - \bar{O}|)^2} \quad (7)$$

P_i is the value obtained from the model, O_i is the observed value, $\bar{O}$ is the average observed value. One indicates a perfect match, and 0 indicates no agreement.

RESULTS AND DISCUSSION

During a given day, Himawari-8 SST data comprise 144 observations, and 3 observations are unavailable. Surface currents are estimated from SST data every 10 minutes resulting in an estimated 140 data. The HF radar data per day includes 67, on July 29, 2022 observations. The data were obtained after manual selection, and time matching between estimated and observation data were performed. A total of 59 data were obtained for July 29, 2022. A validation process is then conducted based on this data. The estimation data from Himawari-8 and HF radar are averaged every 20 minutes over 24 hours.

Ocean surface currents are evaluated by comparing the estimated data to the observation data for the U and V components. Component U represents the current component in a west-east direction, while component V represents the current component in a north-south direction. Regarding spatial resolution, the HF radar grid is 1 km large, and the Himawari output PIVlab grid is 3.8 km large. In the following Step, the HF radar grid is adjusted to the Himawari grid to reduce errors resulting from a higher spatial resolution adjustment. The objective is to obtain spatial validation results for each U and V component based on statistical bias, root mean square error, and the Willmott index.

Figure 3 presents the bias error values for July 29, 2022. The black dot on the left is the HF radar location at LAWA, and the KARA is on the right. From the figure, it can be seen that the HF radar range to the north area is wider than the south area. If calculated based on the grid area, the HF radar range to the northern area is around 22.8 km. The field in the opposite direction is around 7.6 km. Based on Figure 3, the bias error for the U component is generally more significant than that for the V component. In the U component, the maximum bias error is concentrated north of the HF radar, with a value range of 0.4 – 0.5 ms^{-1}. This condition looks different for the V component, where the bias error is lower in the same area, with values ranging from 0 – 0.2 ms^{-1}.

The most significant bias error of the V component is in the most distant area or the outermost area of the HF radar. This bias error has a value of 0.2 – 0.3 ms^{-1}. In the meantime, in the area south of the HF radar location, the U component shows a lower bias error than in the area to the north, with values ranging from -0.2 – 0.2 ms^{-1}. The V component shows slightly different conditions. The V component in this area has a bias error ranging from -0.4 – 0 ms^{-1}. The same is true for the northern area, where the bias error in the V component appears in the outermost area of the HF radar range. The area between LAWA and KARA radar HF also shows that the bias error of the U component is higher than that of the V component with values of 0.1 – 0.4 ms^{-1} and -0.2 - 0 ms^{-1}, respectively, for the U and V components.

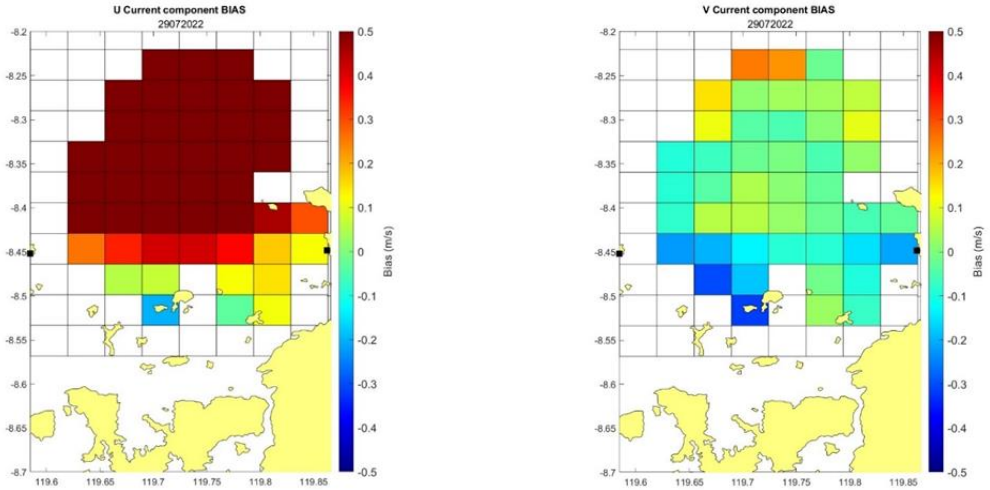

(a) (b)

Figure 3. Bias error of the daily average of data every 20 minutes. Calculated for the U and V components on July 29, 2022, in the HF radar coverage area (black dots are HF radar point locations, LAWA on left and KARA on the right).

On the other hand, an accuracy assessment is also conducted by calculating the RMSE. RMSE estimates the mean difference between prediction and observational values. A lower RMSE value indicates that the predictions are more accurate. As with the bias error, the RMSE of the U component is generally more significant than the RMSE of the V component, as shown in Figure 4. Grids in both the north and south areas of the HF radar tend to have a large RMSE of 0.5 ms^{-1} for the U component. The lowest RMSE is observed on the outermost grid around Sebayur Island at 0.3 - 0.35 ms^{-1}. A similar condition is also seen for the V component, where most of the validation area, especially the northern area, shows a large RMSE with a value reaching 0.5 ms^{-1}. The minimum RMSE for the V component is observed at a location close to the KARA HF radar (around 3-8 km) with a value of around 0.15 – 0.3 ms^{-1}.

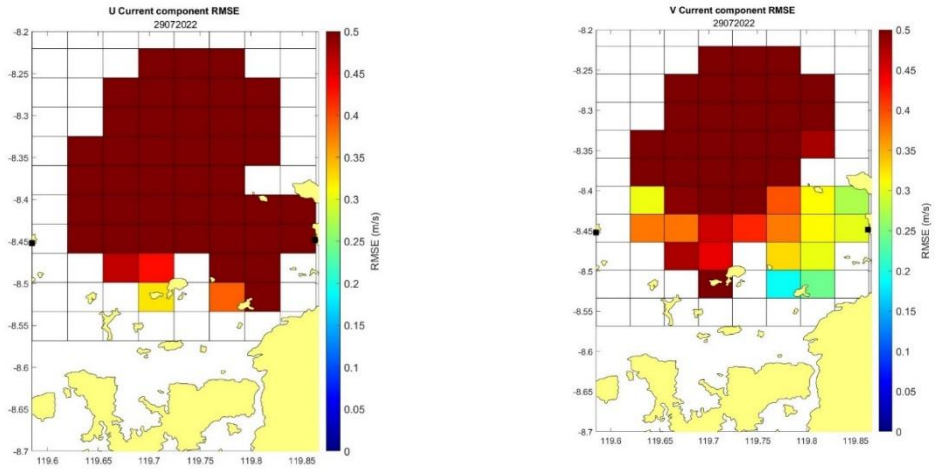

(a) (b)

Figure 4. RMSE of the daily average of data every 20 minutes. Calculated for the U and V components on Jul 29, 2022, in the HF radar coverage area (black dots are HF radar point locations, LAWA on the left and KARA on the right).

Furthermore, the accuracy calculation also uses the Willmott index of agreement. This index calculates the fit of measurement results between Himawari and HF radars for the ocean current parameters U and V components, respectively. The results of the Willmott index are shown in Figure 5. As the Willmott index is 0 - 0.1 for most U components, there is little agreement between Himawari and HF radar measurements of ocean current U components. Meanwhile, better results are shown by the V component, where the northern area lacks agreement with values ranging from 0 – 0.1, while the southern area has a better deal with values ranging from

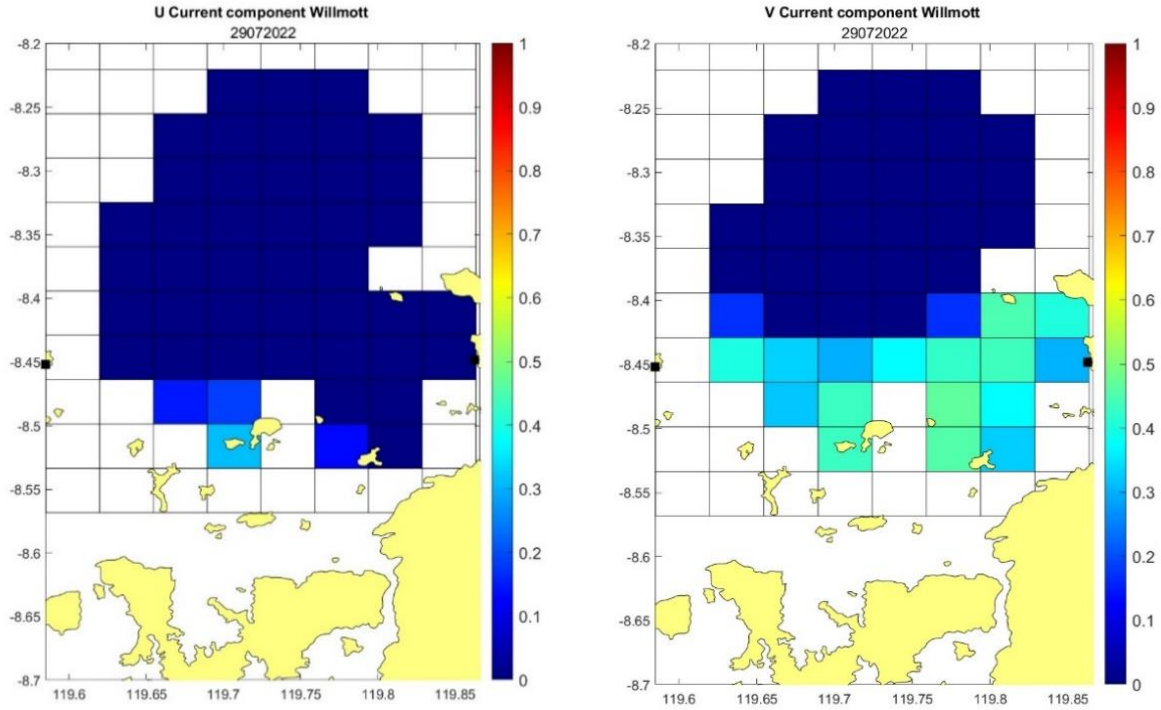

0.3 – 0.5.

(a) (b)

Figure 5. Willmott agreement index of the daily average of data every 20 minutes. Calculated for the U and V components on Jul 29, 2022, in the HF radar coverage area (black dots are HF radar point locations, LAWA on the left and KARA on the right).

Estimating surface current velocity using SST data and the PIV method was performed at 10-minute intervals on each selected research date. Estimation data is then displayed as a current rose to describe the average percentage of surface current movement in a day. This is done in each area of the Flores Sea. The current rose is a diagram showing the average proportion of the current setting toward each significant compass point in a specified maritime area. The effect of tidal currents was not considered in this analysis due to their negligible effect on the open sea and processing of the data in the context of daily averages.

Since the study area is quite large and the surrounding seas have different influences, the study area between 7.5° – 8.5° South and 119°-123° East is divided into three parts, including the western part (area 1) covering coordinates 7.5°–8.5° S and 119°–120° E; the central part (area 2) includes coordinates 7.5°–8.5° S and 120°–122° E; and the eastern part (area 3) includes coordinates 7.5°– 8.5° S and 122°–123° E. The movement of surface currents in each area is then displayed as a current rose every 3 hours. The time classification for the analysis is as follows: 00-03 UTC and 03-06 UTC represent the morning; 06-09 UTC and 09-12 UTC

represent noon; 12-15 UTC and 15-18 UTC represent nighttime; 18-21 UTC and 21-24 UTC represent early morning.

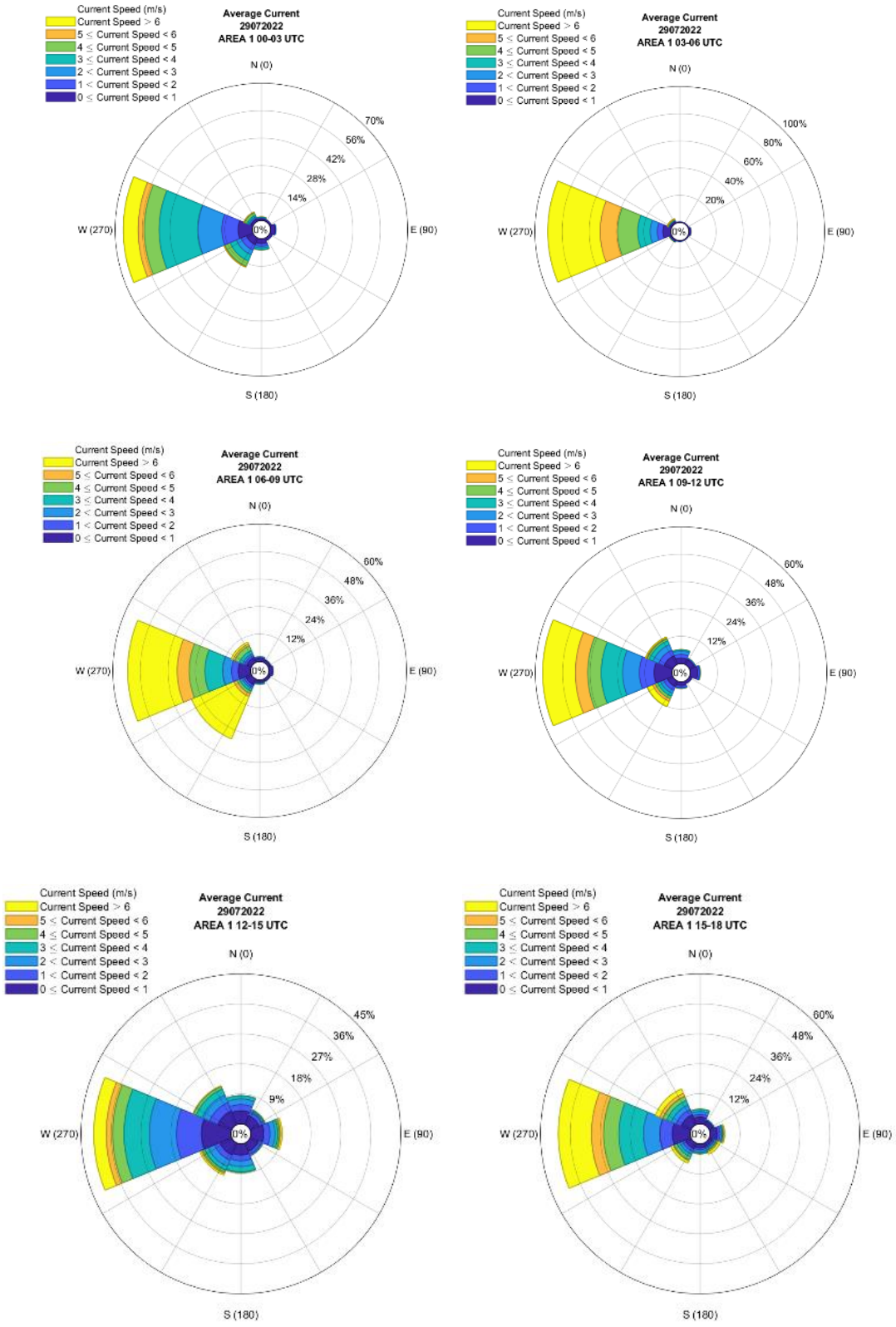

Figure 6. Current Rose of estimated surface current from Himawari-8 SST Data. This visualization shows the surface current distribution every 3 hours on July 29, 2022, in the western Flores Sea (area 1) at 00 – 18 UTC.

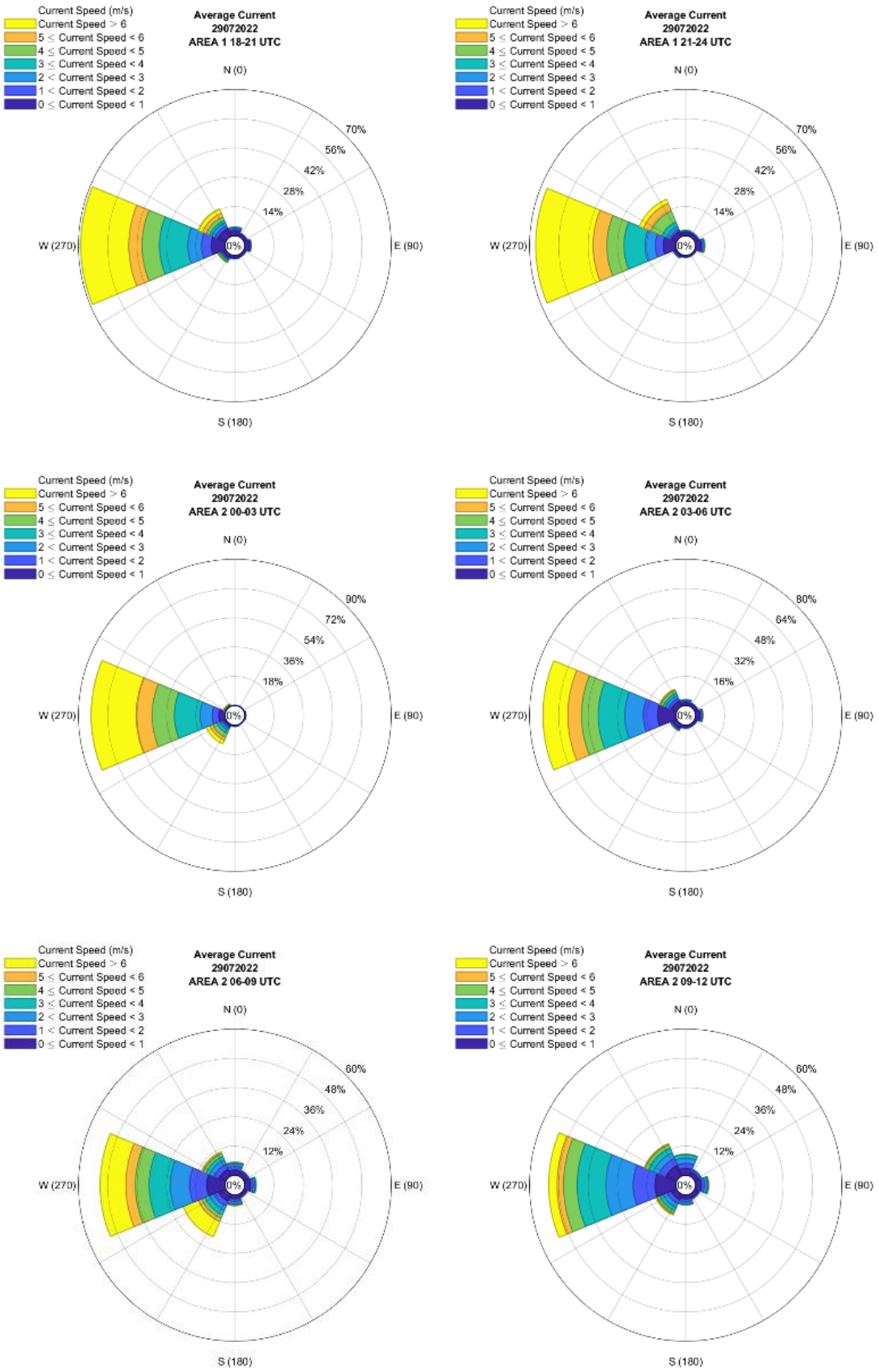

Figure 7. The same as Figure 6, but for the western Flores Sea (area 1) at 18 – 24 UTC; in the central Flores Sea (area 2) at 00 – 12 UTC.

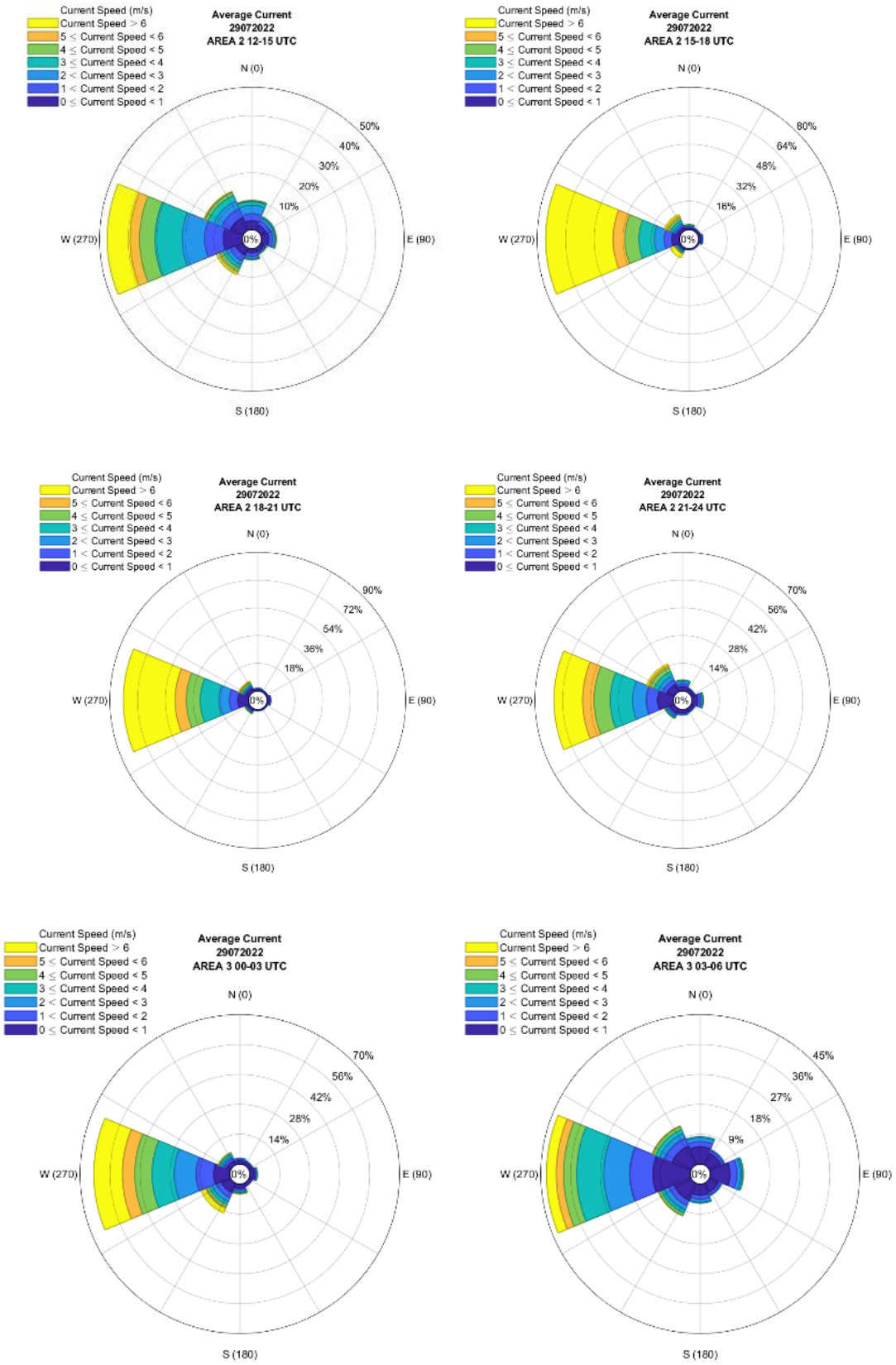

Figure 8. The same as Figure 6, but for the central Flores Sea (area 2) at 12 – 24 UTC; in the eastern Flores Sea (area 3) at 00 – 06 UTC.

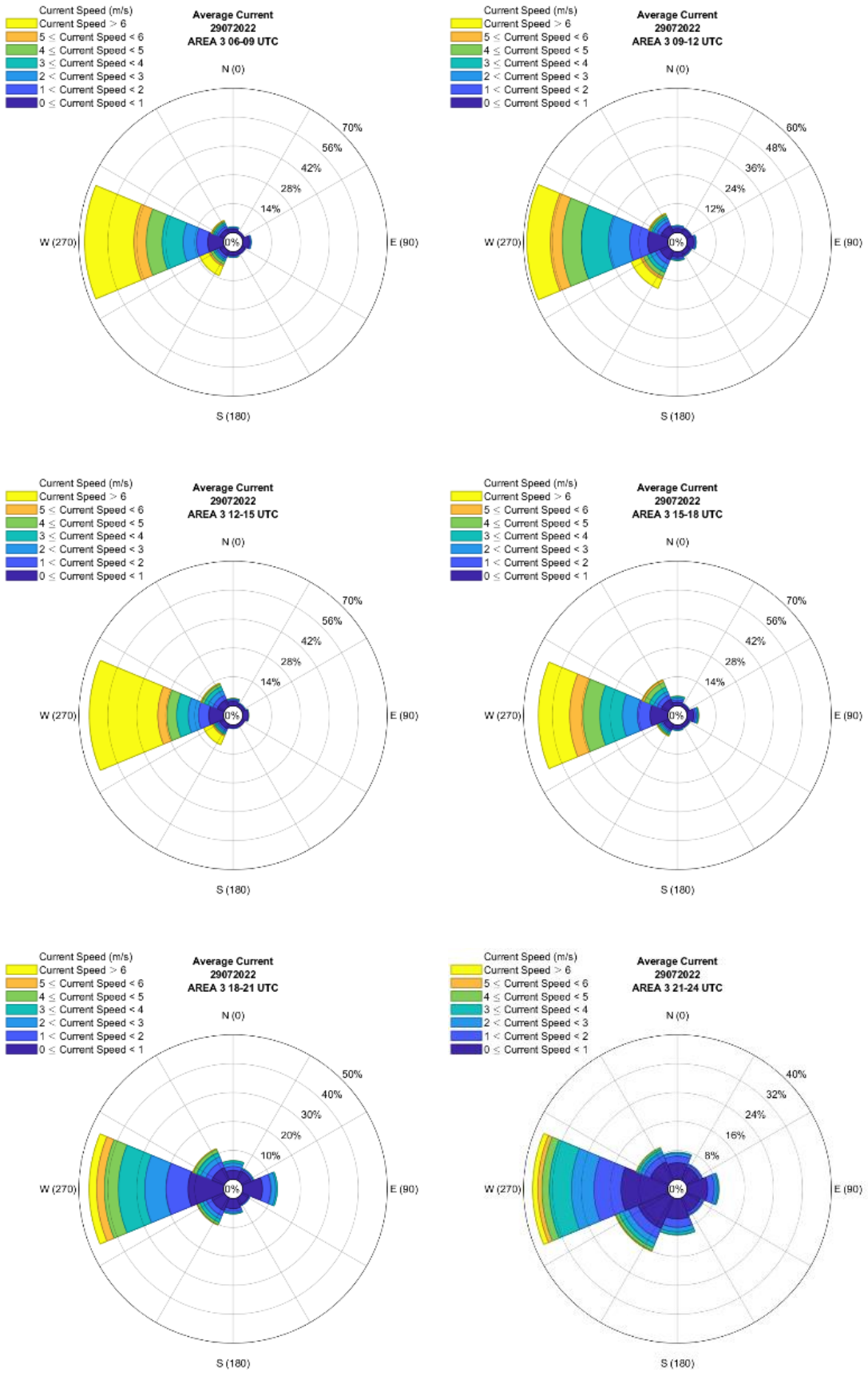

Figure 9. The same as Figure 6, but for the eastern Flores Sea (area 3) at 06 – 24 UTC.

Overall, the estimated ocean surface currents for July 29, 2022, have a daily average distribution of surface currents that are dominantly moving west. This is with a total percentage of nearly 60%. About 40% of surface current flow occurs in other directions, such as the Northwest and Southwest, but is still dominated by the westerly direction. Surface currents are estimated to move at 0-21 ms^{-1} speeds. More detailed results in each area will be explained and shown in Figure 6, Figure 7, Figure 8, and Figure 9.

The daily distribution of ocean surface currents in the western part of the Flores Sea is generally dominated by movements in the zonal direction (West – East) in the morning, afternoon, evening, and early morning. In the morning, ocean surface currents move towards the west with a percentage of around 60-90%. Ocean surface currents do not vary significantly in other directions besides westward. Conditions during the day show a similar pattern as in the morning, where ocean surface currents dominate the west with a percentage of 50-60%. Only minor differences are observed in ocean surface current movement direction at night, especially between 12-15 UTC. While the currents are still prevalent in the west (40-50%), they also increase in the meridional direction (North-South) and the opposite direction, i.e., toward the East. In the early morning, the conditions were identical in the morning and afternoon. Ocean surface currents move westward dominantly with a 60-70% percentage. The maximum flow occurs during the day at speeds ranging from 14-21 ms^{-1}.

Similar to conditions in the western part of the Flores Sea, where surface currents generally travel in a zonal direction to the west. In the morning, 65-85% of ocean surface currents moved toward the west. During the day, there was a variation in meridional flow. Despite this, it still had 40-50% dominance towards the west. These conditions continued into the evening at 12-15 UTC. Later, surface currents again showed a pattern similar to morning conditions and continued until the early morning hours. The percentages indicate that surface currents move west by 55-85%. The maximum flow occurs during the day at speeds ranging from 12-16 ms^{-1}.

The eastern part of the Flores Sea also shows the dominance of movement in a zonal direction, specifically towards the west, similar to the western and central regions. In the morning and early morning, the dominant current moves to the west with a 35-60% percentage. There is increasing variation in surface current movement in the opposite direction, i.e., towards the East in the early morning hours. However, there is a slight difference where surface currents vary more throughout the day and night in the west and central parts. In the East, these conditions occur in the morning, with clearer meridional (north-south) variation. Day and night, the pattern remains stable with a dominant westward direction, and the percentage ranges from 56-70%. Maximum flow occurs during the day at speeds ranging from 12-16 ms^{-1}.

This study shows that accuracy results vary in the validation area, particularly along the Flores HF radar range. The area to the south of the HF radar locations generally has better prediction results for surface currents than the northern area based on bias, RMSE, and the Willmott agreement index. Considering its location, the north part is adjacent to the Flores Sea open sea. In contrast, the southern part is surrounded by the Komodo National Park archipelago, so many small islands are found there. Because surface current velocity prediction is based on the SST distribution, we need to review the SST conditions. The SST distribution around open sea generally fluctuates more than in narrow sea. This condition causes the estimated surface current in the open sea in the north to produce a higher value than the area in the south. Narrow sea have a more uniform SST distribution with lower predictive values. This explains why narrow sea are more accurate. This is because there are many calm currents in confined areas,

which can also be predicted well by the PIV method. Meanwhile, the open sea produces a significant predictive value, so there is a big difference from the observed value.

Based on identification carried out at the research location, it is clear that most surface currents with high speeds occur in open sea areas at the study times. These currents have a speed above than 6 ms^{-1}. This study demonstrates that open sea and deep water are less unreliable for applying the PIV method. Meanwhile, narrow strait and coastal areas which are shallow waters have an estimated surface current velocity of less than 6 ms^{-1}. This area provides a more reasonable estimate of surface current velocity than other areas. So, based on this research, this area is more reliable for the PIV method.

Furthermore, the validation results of the V component, which is better than the U component in the HF area of the radar, indicate that the predominant direction of current movement in this area is north-south. Ocean currents do not move zonally but meridionally when passing through narrow straits due to obstructions from land to the West and East. There are also differences in tides and bathymetry between the Flores Sea in the north and the Indian Ocean in the south. These differences influence surface current meridionally movement.

The results of estimating the motion of surface currents from the SST data and the PIV method produced in this study follow the previous studies that the Australian monsoons strongly influence the motion of surface currents in the Flores Sea[29-30], in particular. Referring to previous studies, ocean surface currents will move eastward. As previously mentioned, surface currents are dominant in zonal motion. On Jul 29, 2022, the Australian monsoon winds blew from the East, moving surface currents to the west, which can be seen in the resulting current rose that surface currents generally move westward in the western, central, and eastern parts of the Flores Sea.

CONCLUSION

According to Himawari-8 SST data, the accuracy of ocean surface currents in the Flores Sea is generally higher for the north-south current component than for the east-west current component. A high V component validation result was found around the KAWA HF radar in the south area. Daily average distributions of the Flores Sea ocean surface currents observed from the Himawari-8 SST are dominated by` east-west (zonal) currents. The Australian monsoons significantly influence them. During the study period in July, surface currents appeared dominant to the west due to the influence of Australian monsoon winds. The study shows that there are high biases in sea surface current calculation in some part of the Flores Sea. This may be attributed to several factors, including cloud cover, extreme dynamic SST caused by upwelling and downwelling, lack of spatial resolution of Himawari-8 or unrealistic PIV methods. These factors need to be investigated in the future.

There is still a great deal of research to be done regarding the adjustment of PIV calculation methods, such as interrogation windows, post-processing, etc., to produce better data accuracy estimations. In order to collect a better understanding of the quality of the estimated data produced, the addition of the research period is necessary. There is a need to separate residual current components from radar data in order to use HF radar data as validation data. It is necessary to consider the observation data from other instruments, such as ADCP, drifter, and satellite altimetry in order to make up for the shortcomings of HF radar.

ACKNOWLEDGMENTS

The authors thank data providers, namely JAXA Himawari Monitor System, Japan, and the Maritime Meteorological Center of BMKG Jakarta.

REFERENCES

1. Röhrs, J., Sutherland, G., Jeans, G., Bedington, M., Sperrevik, A. K., Dagestad, K. F., ... & LaCasce, J. H. 2023. Surface currents in operational oceanography: Key applications, mechanisms, and methods. *Journal of Operational Oceanography*, *16*(1), 60-88.
2. Choi, J. M., Kim, W., Hong, T. T. M., & Park, Y. G. 2021. Derivation and Evaluation of Satellite-Based Surface Current. *Frontiers in Marine Science*, *8*, 695780.
3. Ghalenoei, E., & Hasanlou, M. 2017. Monitoring of sea surface currents by using sea surface temperature and satellite altimetry data in the Caspian Sea. *Earth Observation and Geomatics Engineering*, *1*(1), 36-46.
4. Klemas, V. 2012. Remote sensing of coastal and ocean currents: An overview. *Journal of Coastal Research*, *28*(3), 576-586.
5. Taniguchi, N., Kida, S., Sakuno, Y., Mutsuda, H., & Syamsudin, F. 2019. Short-term variation of the surface flow pattern south of Lombok Strait observed from the Himawari-8 sea surface temperature. *Remote Sensing*, *11*(12), 1491.
6. González-Haro, C., Isern-Fontanet, J., Tandeo, P., & Garello, R. 2020. Ocean surface currents reconstruction: Spectral characterization of the transfer function between SST and SSH. *Journal of Geophysical Research: Oceans*, *125*(10), e2019JC015958.
7. Chen, W., Mied, R. P., & Shen, C. Y. 2008. Near-surface ocean velocity from infrared images: Global optimal solution to an inverse model. *Journal of Geophysical Research: Oceans*, *113*(C10).
8. Ciani, D., Rio, M. H., Nardelli, B. B., Etienne, H., & Santoleri, R. 2020. Improving the altimeter-derived surface currents using sea surface temperature (SST) data: A sensitivity study to SST products. *Remote Sensing*, *12*(10), 1601.
9. Kelly, K. A. 1989. An inverse model for near-surface velocity from infrared images. *Journal of Physical Oceanography*, *19*(12), 1845-1864.
10. Vigan, X., Provost, C., Bleck, R., & Courtier, P. 2000. Sea surface velocities from sea surface temperature image sequences: 1. Method and validation using primitive equation model output. *Journal of Geophysical Research: Oceans*, *105*(C8), 19499-19514.
11. Cote, S., & Tatnall, A. R. 2007. The use of the Hopfield neural network to measure sea-surface velocities from satellite images. *IEEE Geoscience and Remote Sensing Letters*, *4*(4), 624-628.
12. Marghany, M., Hashim, M., & Cracknell, A. P. 2008. Hopfield neural network for sea surface current tracking from Tiungsat-1 data. In *Computational Science and Its Applications–ICCSA 2008: International Conference, Perugia, Italy, June 30–July 3, 2008, Proceedings, Part II 8* (pp. 950-958). Springer Berlin Heidelberg.
13. Kusnanti, E. A., Rini Novitasari, D. C., Setiawan, F., Fanani, A., Hafiyusholeh, M., & Permata Sari, G. I. 2022. Predicting Velocity and Direction of Ocean Surface Currents using Elman Recurrent Neural Network Method. *Journal of Information Systems Engineering & Business Intelligence*, *8*(1).
14. Kim, H. Y., Park, K. A., Kim, H. A., Chung, S. R., & Cheong, S. H. 2020. Retrievals of Sea Surface Current Vectors from Geostationary Satellite Data (Himawari-8/AHI). *Asia-Pacific Journal of Atmospheric Sciences*, *56*, 249-263.
15. Zhu, Z., Geng, X., Li, S., Xie, T., & Yan, X. H. 2020. Ocean surface current retrieval at Hangzhou Bay from Himawari-8 sequential satellite images. *Science China Earth Sciences*, *63*, 1026-1038.

16. Perkovic, D., Lippmann, T. C., & Frasier, S. J. 2009. Longshore surface currents measured by Doppler radar and video PIV techniques. *IEEE transactions on geoscience and remote sensing*, *47*(8), 2787-2800.
17. Rüssmeier, N., Hahn, A., & Zielinski, O. 2017. Ocean surface water currents by large-scale particle image velocimetry technique. In *OCEANS 2017-Aberdeen*, 1-10. IEEE.
18. Supriyadi, E., Hidayat, R., Santikayasa, I. P., & Ramdhani, A. 2021. An Analysis of Surface Ocean Currents from HF Radar Measurements in the Bali Strait and the Flores Sea, Indonesia. *International Journal on Advanced Science, Engineering and Information Technology*, *11*(4), 1521-1534.
19. Atmadipoera, A. S., & Hasanah, P. 2017. Characteristics and variability of the flores itf and its coherence with the south java coastal current. *Jurnal Ilmu dan Teknologi Kelautan Tropis*, *9*(2), 537-556.
20. Yang, M., Guan, L., Beggs, H., Morgan, N., Kurihara, Y., & Kachi, M. 2020. Comparison of Himawari-8 AHI SST with shipboard skin SST measurements in the Australian region. *Remote Sensing*, *12*(8), 1237.
21. Hsu, T. W., Shin, C. Y., Ou, S. H., & Li, Y. T. 2011. Multi-Cross-Correlation Method in Particle Image Velocimetry. *Journal of Mechanics*, *27*(3), 365-377.
22. Fujita, I., Muste, M., & Kruger, A. 1998. Large-scale particle image velocimetry for flow analysis in hydraulic engineering applications. *Journal of hydraulic Research*, *36*(3), 397-414.
23. Balamurugan, R., & Jeeva, B. 2019. Micron size particle image velocimetry by fast Fourier transform. In *AIP Conference Proceedings* (Vol. 2162, No. 1). AIP Publishing.
24. Nogueira, J., Lecuona, A., Ruiz-Rivas, U., & Rodriguez, P. A. 2002. Analysis and alternatives in two-dimensional multigrid particle image velocimetry methods: application of a dedicated weighting function and symmetric direct correlation. *Measurement Science and Technology*, *13*(7), 963.
25. Stamhuis, E., & Thielicke, W. 2014. PIVlab–towards user-friendly, affordable and accurate digital particle image velocimetry in MATLAB. *Journal of open research software*, *2*(1), 30.
26. Patel, A., Dharpure, J. K., Snehmani, & Ganju, A. 2019. Estimating surface ice velocity on Chhota Shigri glacier from satellite data using Particle Image Velocimetry (PIV) technique. *Geocarto international*, *34*(4), 335-347.
27. Menditto, A., Patriarca, M., & Magnusson, B. 2007. Understanding the meaning of accuracy, trueness and precision. *Accreditation and quality assurance*, *12*, 45-47.
28. Willmott, C. J., Robeson, S. M., & Matsuura, K. 2012. A refined index of model performance. *International Journal of climatology*, *32*(13), 2088-2094.
29. Putriani, P. Y., Atmadipoera, A. S., & Nugroho, D. 2019. Interannual variability of Indonesian throughflow in the Flores Sea. In *IOP Conference Series: Earth and Environmental Science*, *278*(1),012064. IOP Publishing.
30. Havis, M. I., & Yunita, N. F. 2017. Surface Currents in Indonesian Sea Based on Ocean Surface Currents Near–Realtime (Oscar) Data. *Marine Technology for Sustainable Development*, 27-31.